

JGR Solid Earth

RESEARCH ARTICLE

10.1029/2022JB024227

Key Points:

- Coseismic and postseismic surface displacements of the 2018 M_w 7.5 Papua New Guinea earthquake are captured by InSAR
- The depth extent of coseismic and postseismic slip on a flat-ramp fault suggests thick-skinned deformation
- Fault frictional heterogeneity is found based on variable seismic and aseismic slip behaviors of three separated postseismic slip zones

Supporting Information:

Supporting Information may be found in the online version of this article.

Correspondence to:

X. Liu,
xiaogeliu@csu.edu.cn

Citation:

Xu, W., Liu, X., Bürgmann, R., Xie, L., Feng, G., Li, Z., & Wu, L. (2022). Space geodetic evidence of basement-involved thick-skinned orogeny and fault frictional heterogeneity of the Papuan Fold Belt, Papua New Guinea. *Journal of Geophysical Research: Solid Earth*, 127, e2022JB024227. <https://doi.org/10.1029/2022JB024227>

Received 16 FEB 2022

Accepted 10 AUG 2022

Author Contributions:

Conceptualization: Xiaoge Liu
Data curation: Wenbin Xu, Xiaoge Liu
Formal analysis: Wenbin Xu, Xiaoge Liu, Roland Bürgmann, Lei Xie, Guangcui Feng, Zhiwei Li, Lixin Wu
Funding acquisition: Wenbin Xu
Investigation: Wenbin Xu, Xiaoge Liu
Methodology: Xiaoge Liu
Resources: Wenbin Xu, Roland Bürgmann
Software: Wenbin Xu, Xiaoge Liu
Supervision: Wenbin Xu
Validation: Wenbin Xu, Xiaoge Liu, Roland Bürgmann, Lei Xie
Visualization: Xiaoge Liu
Writing – original draft: Xiaoge Liu
Writing – review & editing: Wenbin Xu, Xiaoge Liu, Roland Bürgmann, Lei Xie

© 2022. American Geophysical Union.
All Rights Reserved.

Space Geodetic Evidence of Basement-Involved Thick-Skinned Orogeny and Fault Frictional Heterogeneity of the Papuan Fold Belt, Papua New Guinea

Wenbin Xu¹ , Xiaoge Liu¹ , Roland Bürgmann² , Lei Xie³ , Guangcui Feng¹ , Zhiwei Li¹ , and Lixin Wu¹

¹School of Geosciences and Info-Physics, Central South University, Changsha, China, ²Department of Earth and Planetary Science, University of California, Berkeley, CA, USA, ³Department of Land Surveying and Geo-Informatics, The Hong Kong Polytechnic University, Hong Kong, China

Abstract Knowledge of the fault kinematics underlying the Papuan Fold Belt is important for better understanding the evolution of the orogen, but the active and long-term tectonics of the region remain widely debated. The 2018 M_w 7.5 Papua New Guinea earthquake provides an unprecedented opportunity to probe the active fault structure deep in the Papuan Fold Belt. Here, we use Interferometric Synthetic Aperture Radar data from four ALOS-2 acquisitions to study coseismic and postseismic ground deformation and invert for fault slip models. The results show that the oblique reverse earthquake reactivated a flat-ramp structure and ruptured through most of the crust with the majority of coseismic slip confined between 5 and 25 km. Additionally, we found three separated postseismic slip zones with variable spatial complementarity between coseismic and postseismic slip, dip-slip/strike-slip ratio, and seismic/aseismic budget at three separated postseismic slip zones. Our results demonstrate that thick-skinned tectonics dominate the current state of Papua New Guinea frontal orogen evolution.

Plain Language Summary On 25 February 2018, an M_w 7.5 earthquake struck the central Papua New Guinea Highland. We use Interferometric Synthetic Aperture Radar data (ALOS-2) to study the surface displacements associated with the great earthquake, seismogenic fault geometry, and coseismic and postseismic slip. We find complex seismic and aseismic slip occurred on a flat-ramp structure, which ruptured through most of the crust indicating thick-skinned basement-involved deformation during the earthquake. We also compare the uplift displacements and the topography and local folds, and highlight that thick-skinned tectonics play a significant role in the current frontal orogen evolution of Papua New Guinea.

1. Introduction

The fold and thrust belt of Papua New Guinea (PNG) is one of the most tectonically complex and seismically active arc-continent collision orogens in the world (Baldwin et al., 2012). The Papuan Fold Belt (PFB) is the manifestation of sinistral oblique convergence between the Australian continent and Pacific plate at a rate of ~110 mm/yr (Koulali et al., 2015). Based on GPS deformation measurements, Tregoning et al. (1998) suggest that ~64% of the convergence is accommodated within the PNG mainland. The PNG mainland is commonly subdivided into three major tectonic provinces from southwest to northeast, referred to as the Stable Platform, PFB, and Accreted Terranes (Figure 1). Geologically, the Papuan Basin comprises 7–10-km thick sediments separated from the underlying Australian crystalline basement by Cretaceous Ieru and Toro Formations, Late Jurassic Imburu, Barikewa, and Magobu Formations (mudstone and shale with siltstone), thick Eocene-Late Miocene limestones (Darai Limestone) and Late Miocene to recent clastics (Hill et al., 2010; Mahoney et al., 2017). This sedimentary cover is folded into anticlines, apparent in the topography of the fold belt, some of which host significant hydrocarbon fields (Abers & McCaffrey, 1988; Hanani et al., 2016; Hill et al., 2010; Hobson, 1986; Mahoney et al., 2017).

As one of the youngest folds and thrust belts on Earth (Mahoney et al., 2017), the PFB provides a natural laboratory to explore the structures and kinematics of an active collisional orogen, including the involvement of thin-skinned and thick-skinned tectonics in the deformation. However, the PFB remains one of the least well documented fold and thrust belts due to the dense equatorial jungle and inhospitable, challenging conditions for field access (Hill et al., 2010; Ollarves et al., 2020). The involvement of tectonic thick-skinned basement

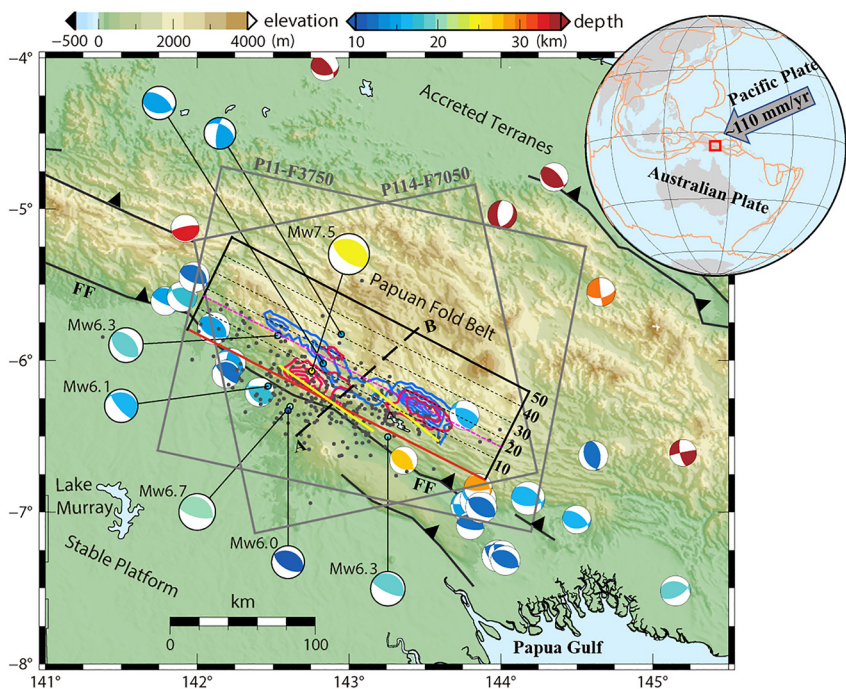


Figure 1. Regional seismotectonic context of the 2018 Papua New Guinea (PNG) earthquake. Smoothed blue and red contours with 1-m and 0.3-m intervals represent coseismic and postseismic slip of the PNG earthquake, respectively. Moment tensors are colored by depth and scaled by magnitude. Magnitude-labeled moment tensors represent the USGS W-phase solutions of the February 25 mainshock at 25.2 km hypocenter depth, and its five large aftershocks ($\geq M_w 6$) including one largest aftershock ($M_w 6.7$, 20.5-km depth) occurred on 6 March 2018. Other moment tensors represent historical events ($\geq M_w 5$) from 1977 to 2018 catalogued at the International Seismological Centre (ISC, <http://www.isc.ac.uk/iscbulletin/search/fmechanisms/interactive/>). Black lines represent the regional active faults from GEM Global Active Faults (<https://github.com/GEMScienceTools/gem-global-active-faults>). Gray dots represent aftershocks (through September 2018) from USGS. Gray boxes indicate the spatial extent of ALOS-2 imagery used in this study and labeled by path and frame number. The black rectangle represents the ground projection of the modeled fault plane with the red solid line indicating its surface trace, dashed lines indicating 10-km depth intervals and pink dashed line indicating transition depth (16 km) between shallow and deep fault parts. Two yellow lines represent the surface traces of two faults used by Chong and Huang (2020). Dashed line is the location of cross-section A–B in Figure 7b. The inset shows the location of the study area and relative plate motion (Koulali et al., 2015) with light yellow lines indicating plate boundaries. FF, Frontal Fault.

faulting structures in the PNG orogen is actively debated. Based on geological maps, geophysical imaging, and well data, Hobson (1986) proposed the dominance of thin-skinned deformation in the evolution of the PNG mountain range. In contrast, Hanani et al. (2016) interpreted seismic reflection profiles to argue for an important role of thick-skinned faulting. This is consistent with the Triassic basement reached in gas well drilling reported by Valenti (1993). In addition, interaction of thin-skinned and thick-skinned faulting processes in PFB has also been proposed (Mahoney et al., 2017; Mason, 1997; Smith, 1990). These existing studies of the PNG mountains are based on well data, topographic information and sparse 2D seismic data that are challenged by several factors, including the complex ray path and energy scattering (poor imaging) related to the thick, intensely karstified limestone (Darai Limestone) found at the surface throughout most of the PFB (Hill et al., 2010; Ollarves et al., 2020). In addition, the uncertainties of structural interpretation based on seismic reflection results increase with depth (Hill et al., 2010). Thus, these existing studies primarily illuminate the shallow faulting structure in the uppermost crust.

Moderate sized thrust earthquakes with minor or moderate strike-slip components are prevalent beneath the PFB (Figure 1). The centroid depths (11–22 km) of three earthquakes located in southeastern PNG near the Gulf of Papua indicate they occurred below the sedimentary section (Abers & McCaffrey, 1988). Mahoney et al. (2017) pointed to the importance of seismogenic structures extending into the basement in the PFB, which is confirmed by the prevalence of centroid depths (12–33 km) of all moderate historical earthquakes (Figure 1). The depth range of these earthquakes encompasses the average crustal thickness of about 35 km beneath the PFB from

Table 1Details of the ALOS-2 SAR Data Used in This Study and Moment Release Contribution of $M_w > 6$ Aftershocks of the $M_w 7.5$ 25 February 2018 Mainshock

Interferograms	Primary (yyyymmdd)	Secondary (yyyymmdd)	Path	Frame	Direction	Bperb (m)	Aftershocks (M_w)	Ratio (%)
CoAT114	20170731	20180226	114	7,050	Ascending	77	6.3 (26 Feb.)	1.1
CoDT11	20180201	20180301	11	3,750	Descending	150	6.3 (26 Feb.), 6.1 (28 Feb.)	1.7
PostAT114	20180226	20180910	114	7,050	Ascending	216	6.1 (28 Feb.), 6.0 (4 Mar.), 6.7 (6 Mar.), 6.3 (7 Apr.)	7.5
PostDT11	20180301	20180816	11	3,750	Descending	60	6.0 (4 Mar.), 6.7 (6 Mar.), 6.3 (7 Apr.)	6

Note. CoAT114 and CoDT11 are the ascending and descending coseismic interferograms, respectively. PostAT114 and PostDT11 are the ascending and descending postseismic interferograms, respectively. Ratio is the moment ratio between the $M_w > 6$ aftershocks (except for the largest M_w 6.7 aftershock) and the total modeled coseismic/postseismic slip (Tables S1 and S4 in Supporting Information S1).

CRUST1.0 (Laske et al., 2013), suggesting that lower-crustal basement-involved faulting accommodates the thick-skinned shortening of crystalline Australian basement beneath the PFB.

On 25 February 2018, the $M_w 7.5$ PNG thrust earthquake struck the PFB, making it one of the largest instrumentally recorded earthquakes to have occurred in the central PNG mountains to date. Moment tensor solutions and aftershock locations indicate that the PNG earthquake ruptured a moderately (30°) northeast dipping thrust plane with a centroid depth of 19.5 km and hypocenter at 25 km (USGS). The depth of this earthquake is much greater than the thickness (7–10 km) of the overlying sedimentary units as defined by Hill et al. (2010) and Mahoney et al. (2017), indicating that it ruptured a basement fault structure. Numerous aftershocks include 175 globally recorded M_w 4.5+ events, including the largest M_w 6.7 aftershock on 6 March 2018 from the USGS catalog. These events provide a unique opportunity to study the fault slip distribution and to explore the fault structure within the central PNG mountain. Using seismic and Interferometric Synthetic Aperture Radar (InSAR) data, Zhang et al. (2020) found that the PNG earthquake was a dissipative and cascading rupture event including three asperities. Wang et al. (2020) found that a four-segment fault slip model best fits the InSAR data suggesting possible strain partitioning in the Papuan Thrust Belt. Based on subpixel offset observations, Chong and Huang (2020) reconstructed the 3D coseismic displacement of the PNG earthquake and modeled the event with two fault segments. Combining seismological and geodetic observations, Mahoney et al. (2021) suggested that the architecture of the northern Australian passive margin plays an important role in the PFB structural style. These existing studies are primarily focused on the observations of surface displacements or coseismic kinematics. They do not examine the postseismic slip characteristics. Except for the study of Mahoney et al. (2021), other studies rarely analyze the associated structural styles, which are also important for understanding the evolution of the PNG orogen, fault frictional properties, and seismic hazard.

In this study, we employ InSAR data to image the coseismic and postseismic displacements caused by the 2018 PNG earthquake. We constrain the geometry, location, and fault slip of the seismogenic fault associated with the mainshock and aftershocks. Our model results allow us to explore the subsurface structures and faulting kinematics beneath the PFB, and to assess the mechanisms that drive the current frontal orogen uplift. Finally, we discuss the dominance of thick-skinned tectonics, the topography building and fold growth, the heterogeneity of coseismic slip with multiple asperities and fault segmentation, and shallow slip deficit (SSD).

2. Coseismic and Postseismic InSAR Observations

2.1. InSAR Data Processing

The challenging conditions in the PFB make the weather-independent SAR satellite data especially important for studying the 2018 PNG earthquake. The L-band SAR data acquired by the Japan Aerospace Exploration Agency's ALOS-2 satellite provide a unique opportunity to quantify surface displacements of the PNG earthquake and to constrain the activated fault structures beneath the PFB. Using the Gamma software (Wegmüller et al., 2016), we constructed coseismic and postseismic interferograms with the primary and secondary Single Look Complex products from ascending and descending tracks with different viewing geometries (Table 1). After high-accuracy coregistration of the primary and secondary scenes, each interferogram was sampled to 30 m, and the 30 m

Shuttle Radar Topography Mission digital elevation model (Farr et al., 2007) was used to remove the effect of topography. Then the interferograms were filtered using an improved power spectrum filter to minimize the phase noise (Li et al., 2008) and unwrapped using a minimum cost flow method (Chen & Zebker, 2001). After phase unwrapping, we geocoded the unwrapped interferograms to World Geodetic System 1984 coordinates. As the study area is located in the PNG mountain belt with a tropical climate, atmospheric model data from the Generic Atmospheric Correction Online Service for InSAR (GACOS) were used to mitigate contributions of tropospheric delay (Yu et al., 2018) (Figure S1 in Supporting Information S1). Several large aftershocks contribute to deformation in both coseismic and postseismic interferograms, but the moment release of these large aftershocks is not comparable (<10%) to the coseismic and postseismic moment release (see Table 1). Therefore, we focus mainly on the role of the largest M_w 6.7 aftershock and early afterslip.

2.2. Coseismic and Postseismic Deformation

Coseismic interferograms of the PNG earthquake show relatively well-defined surface displacements along the southwestern foreland boundary of the PFB (Figure 2 and Figure S2 in Supporting Information S1). Due to the limited revisit frequency of current SAR satellites, the interferograms that are dominated by coseismic fault slip and formed by the shortest time interval covering the event are referred to as coseismic interferograms. Both ascending and descending coseismic deformation maps cover strike length ~170 km of the PFB and show up to ~1 m surface displacement toward the satellite in the radar line of sight (LOS) (Figure 2 and Figure S2 in Supporting Information S1). There is no obvious range increase in the radar LOS direction (Figure 2 and Figure S2 in Supporting Information S1). This is in contrast to other thrust events on shallowly dipping faults with dip angle of 5°–15° causing a double-lobe deformation pattern with well-resolved uplift and subsidence regions (Elliott et al., 2016; Liu & Xu, 2019), indicating that the PNG earthquake may have ruptured a relatively steep fault beneath the PFB. Similar uplift-dominated deformation patterns of ascending and descending interferograms suggest that the coseismic fault slip may be dominated by thrusting. It should be pointed out that the coseismic interferograms span some larger aftershocks (but not the largest M_w 6.7 on the 6 March, Table 1), whose contributions to the interferometric phase are not separable from the much larger mainshock deformation.

The postseismic displacement maps show clear evidence of the early postseismic (about half a year after the mainshock) deformation transient (Figure 3 and Figure S3 in Supporting Information S1). Postseismic interferograms are referred to as interferograms containing only deformation following the mainshock and span different time intervals. Due to several large aftershocks ($M_w > 6.0$) including the largest M_w 6.7 aftershock on the 6 March following the PNG earthquake (Figure 1), the postseismic deformation contains the contributions of aftershocks, afterslip, and other possible postseismic relaxation processes. Considering that deformation from the large aftershocks is captured by the coseismic and postseismic interferograms (see Table 1), we focus mainly on the role of the largest M_w 6.7 aftershock and early afterslip. Two obvious postseismic deformation zones with a peak value of ~0.5 m LOS decrease are concentrated in the northwestern and southeastern region on the ascending track (Figure 3). These two deformation zones can also be observed on the descending track. The postseismic deformation features a double-lobe pattern, which is clearly different from the corresponding coseismic deformation (Figures 2 and 3). If the postseismic deformation were dominated by subsidence (uplift), the LOS displacement from both ascending and descending tracks would show very similar range increase (decrease), given the imaging geometry of SAR sensors. Thus, ascending and descending postseismic deformation maps show opposite range decrease and increase patterns, indicating that the postseismic transient is dominated by horizontal motions, possibly including contributions from strike-slip component. GNSS-measured shear in the strike direction (Mahoney et al., 2021), supporting long-term oblique strain accumulation due to the oblique plate convergence.

3. Coseismic and Postseismic Slip Inversion

3.1. Nonlinear Fault Geometry Inversion

Before performing fault geometry inversion, we downsampled the full-resolution interferograms to a computationally tractable size (~370 datapoints for each data set) using a quadtree algorithm (Figure S4 in Supporting Information S1; Jónsson et al., 2002). We estimated the covariances of the downsampled data and employed them to weight the observations in the following inversions (Jónsson et al., 2002). We used a single rectangular dislocation model in a homogeneous, elastic, and isotropic half-space (Okada, 1985) and a multipoint particle swarm

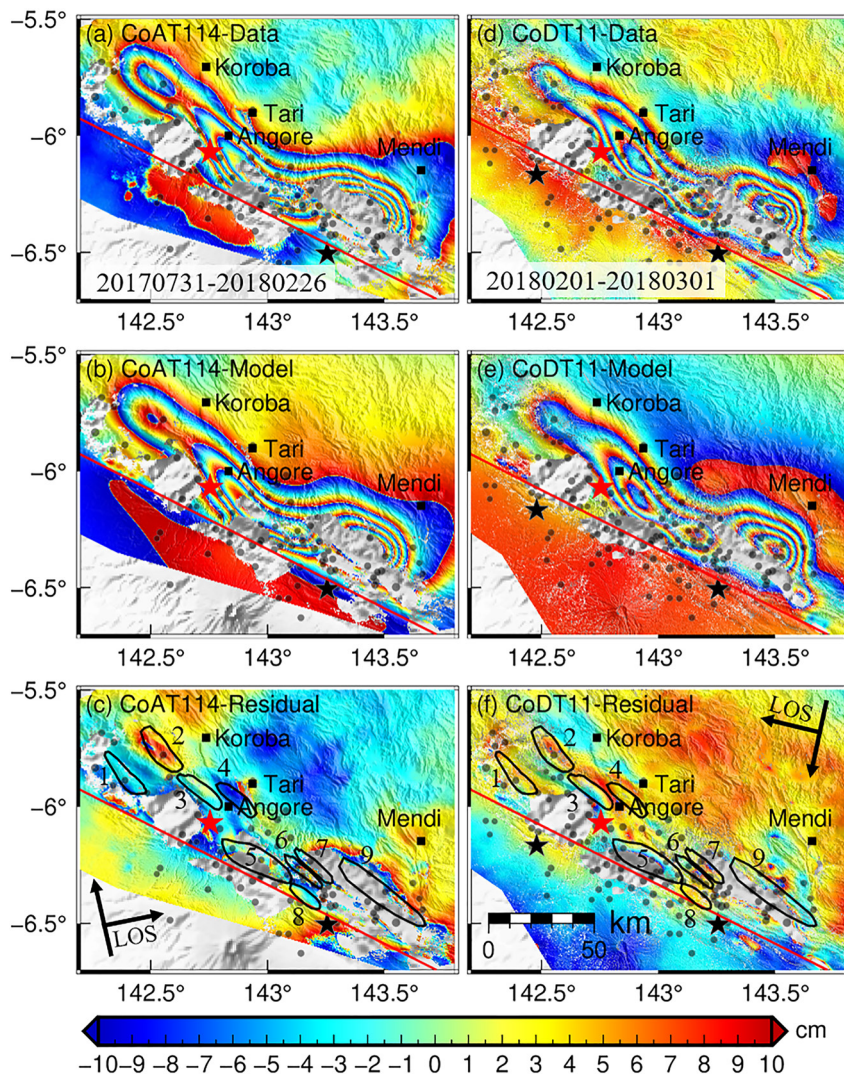


Figure 2. Unwrapped and then rewrapped coseismic interferograms (containing $M_w \geq 6$ aftershocks marked by black stars) with one fringe corresponding to 20 cm in (a–c) ascending and (d–f) descending tracks, respectively. The time spans of interferograms are indicated in the bottom of first row plots. First row: data; second row: model predictions; third row: residuals. Range decrease from warm to cold color; range increase from cold to warm color. Red line and star represent the surface trace of the modeled seismogenic fault and the USGS epicenter, respectively. Gray dots scaled by magnitude are aftershocks during the corresponding time intervals and black squares represent main towns. Numbered black polygons in (c) and (f) delineate the extents of antecedent ranges called (1) Juha, (2) Lavani, (3) Hides, (4) Angore, (5) Mananda, (6) Moran, (7) Paua, (8) Agogo, and (9) Kutubu, respectively.

optimization approach (Feng & Li, 2010) to determine the fault geometry parameters (i.e., location, length, width, strike angle, dip angle, rake angle, and uniform slip). To better cover the solution space and quantify the associated uncertainties, we applied relatively loose search bounds for the fault parameters according to prior knowledge (e.g., focal mechanisms from USGS/GCMT/published literature) (Tables S1 and S2 in Supporting Information S1). The optimal fault parameters and their uncertainties are determined by the Monte Carlo strategy (Xu, 2017). During the model optimizations, 500 perturbed data sets were generated by adding random Gaussian white noise with a standard deviation set as the root-mean-square (RMS) based on each residual data set (Figure S4 in Supporting Information S1). Subsequently, we inverted the perturbed data and obtained a set of model solutions. The solution set was binned into histograms and fit by a Gaussian function to estimate the parameters' 1σ uncertainties (Figure S5 and Table S1 in Supporting Information S1). Although some common trade-offs are observed between the fault parameters such as the proportional relationships between the fault length, width, and slip, the model uncertainties are relatively small, and the moment magnitudes calculated from the respective

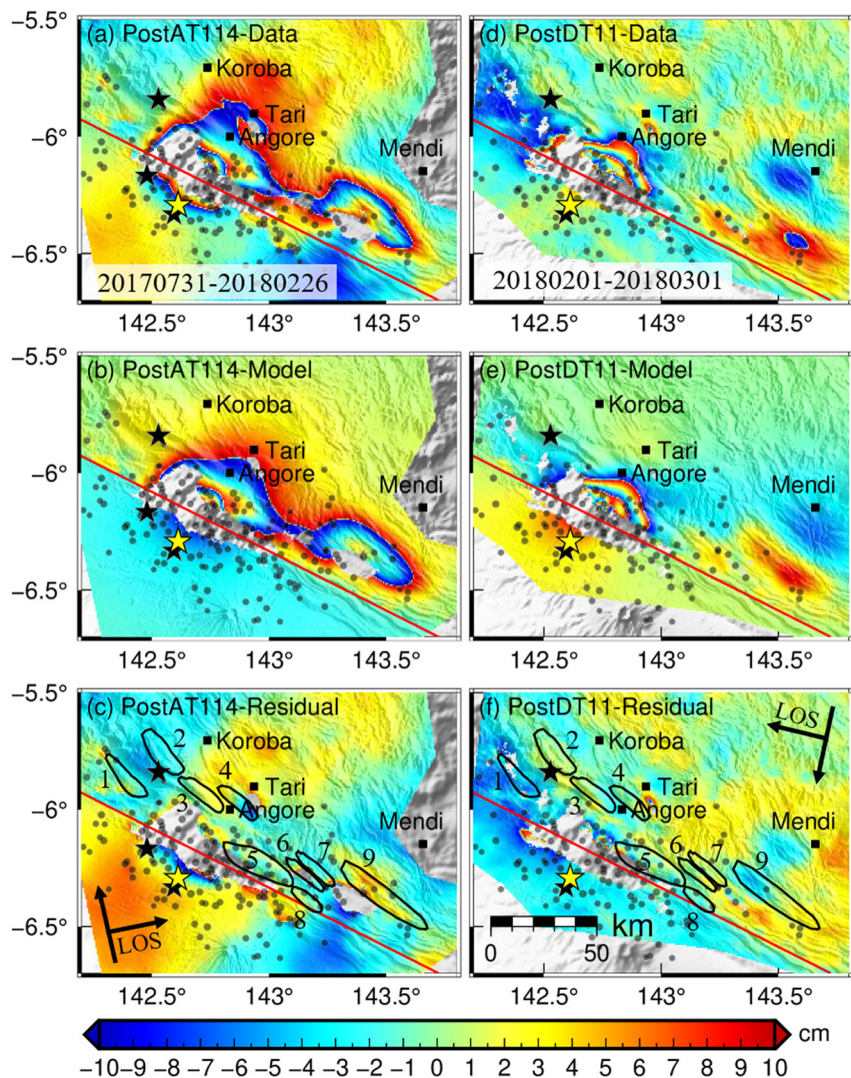


Figure 3. Similar to Figure 2 but for postseismic data and modeling results. The yellow and black stars represent the epicenters of the largest M_w 6.7 aftershock and other $M_w \geq 6$ aftershocks during the corresponding time intervals.

fault length, width, and slip remain similar (Table S1 and Figure S5 in Supporting Information S1). The optimal uniform slip model is 144-km long and 36.5-km wide with a strike angle of 297° , a dip angle of 27° , and a rake (96°) close to pure thrusting. These estimated fault parameters are generally consistent with those reported by other sources (Table S1 in Supporting Information S1).

3.2. Coseismic Distributed Slip Inversion

To check the subsurface fault geometry in the dip direction and resolve a more detailed slip distribution, we design a nonplanar fault structure with different shallow and deep dip angles, fixed fault strike (297°), and extended fault length (250 km) and depth (50 km). Then a 3-D grid search method is used to find the optimal results for the shallow dip angle (search interval 17° – 37°), the deep dip angle (search interval 20° – 60°), and the transition depth (search interval 2–30 km) between these two connected fault sections, involving a total of 3,465 model runs. During the reversion of 3-D grid search, an automated fault discretization method was adopted to invert the detailed coseismic slip model (Barnhart & Lohman, 2010). This approach iteratively discretizes the fault plane to account for the spatial variations of model resolution. To stabilize the slip estimation, the higher order Tikhonov Regularization strategy was adopted, and the regularization factor was determined by using the $\sqrt{R_i}$ strategy to

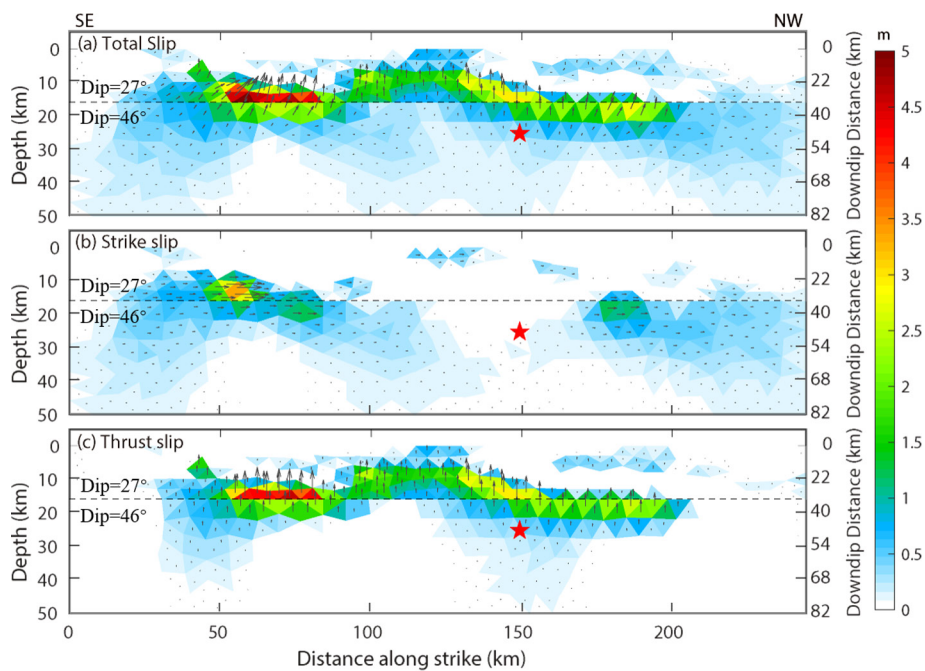


Figure 4. Results of the distributed coseismic slip inversion. (a) Total coseismic slip, (b) strike-slip component, and (c) thrust-slip component. Red star represents the USGS hypocenter of the 2018 Papua New Guinea (PNG) earthquake. Black arrows indicate the slip vector. Gray dashed lines are the 16 km transition depth separating shallow (27°) flat and deep ramp (46°) fault segments.

balance the perturbation error (the influence of observation noise on inversion results) and regularization error (the difference of noise-free observations and regularized model results) (Barnhart & Lohman, 2010).

The 3-D grid search results show that the optimal shallow dip angle of 26.6° is well constrained (black star in Figure S6 in Supporting Information S1). The overall deep dip angles of solutions with low RMSs are larger than 40° ; however, the optimal deep dip angle of 45.7° is not as well constrained as the shallow dip angle. The optimal transition depth between the shallow and deep fault parts is about 16 km. This indicates a flat-ramp fault structure beneath the PFB, which is consistent with the observation that fault dips are often lower in the sedimentary cover than in the deep basement (Mahoney et al., 2017). In terms of the residuals' RMS, the RMS of this model is substantially lower ($\sim 35\%$) than the results for a single plane fault (Figure S6 in Supporting Information S1). In addition, this kind of flat-ramp structure is similar to that found beneath the Himalaya and Zagros orogens (Barnhart et al., 2018; Elliott et al., 2016), although the dip angles here are much larger on both shallow and deep fault segments.

The coseismic slip inversion on flat-ramp fault configuration results indicate that the PNG earthquake ruptured on a fault structure with a length of ~ 150 km beneath the PFB (Figure 4). The PNG earthquake rupture propagated ~ 50 km to the northwest and ~ 100 km to the southeast from the USGS hypocenter. The complex bilateral rupture characteristics captured by the coseismic slip model are in agreement with seismic back-projection results that track the source of high-frequency radiation during the rupture (Zhang et al., 2020). No obvious shallow (0–5 km in depth) coseismic slip suggests that the PNG earthquake may not have ruptured the surface (Figure 4), which is in line with no clear discontinuities in the InSAR coseismic data (Figure 2). However, patches of shallow slip inverted from subpixel offset data with large uncertainty (up to 0.8 m) suggest possible local near-surface faulting (Chong & Huang, 2020, Figure 1). Coseismic slip (>0.5 m) mainly concentrates at 5–25 km in depth, and the maximum total slip (4.9 m) from the preferred slip model is located at a depth of ~ 15 km (Figure 4a). The coseismic fault slip is dominated by thrust slip; however, confined regions located at the southeastern and northwestern ends of the rupture zone show large left-lateral slip with a peak value of about 3 m (Figure 4b). This is supported by oblique horizontal GNSS displacements characterized by a dominant fault-normal component and moderate fault-parallel motions (Mahoney et al., 2021).

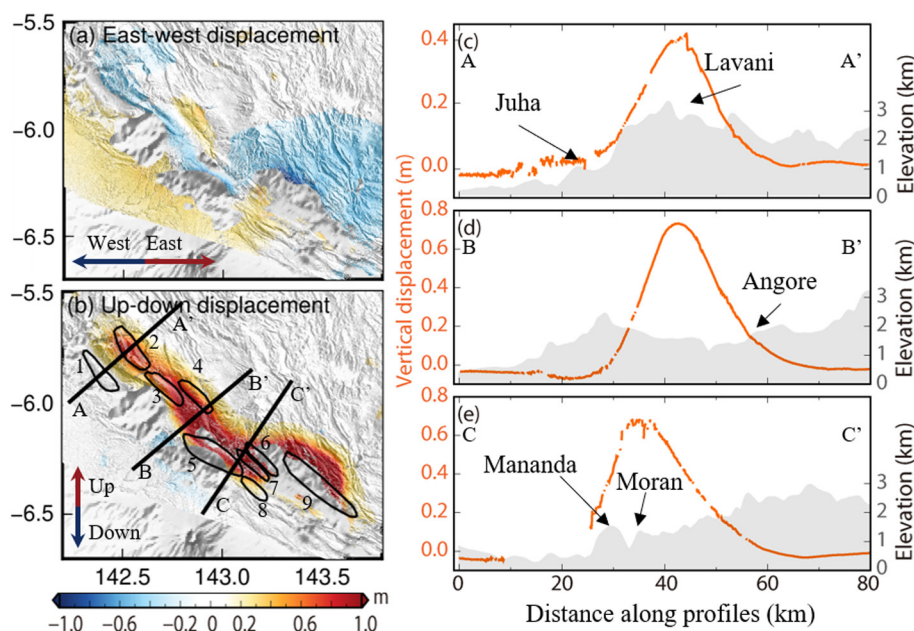


Figure 5. Quasi-2D coseismic ground deformation maps. (a) East-West displacement map; (b) vertical displacement map. Vertical deformation (orange lines) along profiles A–A'(c), B–B'(d), and C–C'(e) in comparison with topography (gray outlines). Names in (c)–(e) marked several anticlines.

Although the exact fault trace of the seismogenic fault is not available, the coseismic slip model suggests one continuous primary fault (Figure 4a) or up to a two-segment rupture trace based on the strike-slip component (Figure 4b), indicating at most one major step-over along the ~150 km rupture zone. This indicates a low step-over density (number of step-overs per kilometer along strike is $\leq 10^{-2}/\text{km}$), implying a relatively mature fault structure hosting the 2018 PNG earthquake, given the scaling relation between segmentation and fault structural maturity (Manighetti et al., 2021). In addition, the ratio between the maximum slip (~5 m) and the rupture length (~150 km) indicates a high degree of structural maturity of the faults (Manighetti et al., 2007; Figure S7 in Supporting Information S1).

The predicted displacements from the best-fitting model explain both ascending and descending coseismic observations well with RMSs of ~6.0 cm for the ascending and descending InSAR data sets (Figure 2 and Figure S2 in Supporting Information S1). The residuals may result from the combined contributions of interferogram decorrelation, residual atmospheric artifacts, up to 6 days of unmodeled early postseismic deformation, possible multisegments faulting along strike and inelastic deformation (e.g., localized folding, landslides, or liquidation). We used an average shear modulus of 33 GPa according to the CRUST1.0 model (Laske et al., 2013), and calculated a geodetic moment (M_0) as $\sim 2.82 \times 10^{20} \text{ Nm}$, which is equivalent to M_w 7.57, which is comparable with other studies (Table S1 in Supporting Information S1). Our estimated coseismic slip distribution and moment magnitude of M_w 7.57 is comparable with those reported in previous studies using geodetic and/or seismological data set (Table S1 in Supporting Information S1).

We decompose the quasi-2D (two-dimensional) coseismic ground deformation fields from the ascending and descending coseismic interferograms, neglecting the North-South motions due to their much smaller contribution to the LOS compared to the East-West and Up-Down components (Hu et al., 2014). The decomposed 2D displacement maps show that the coseismic ground deformation is dominated by vertical displacements (Figure 5), which is consistent with the inverted relatively steep dip angle of the coseismic rupture. Comparing the vertical coseismic displacements and topography, we found the vertical displacements are positively related to the frontal orogen anticlines and associated topography (Figures 5b–5e), indicating that the 2018 PNG earthquake raised the frontal PFB with a maximum uplift of about 1.2 m (Figure 5b). Considering that the main uplift is close to anticinal structures hosting oil and gas fields (Figures 5b–5e) (Hanani et al., 2016; Hill et al., 2010), we suggest that great earthquakes play an important role in structural growth and raising of topography in the fold and thrust belt. Additionally, a fault section (flat) with a low dip angle (5°–7°) is required to explain the

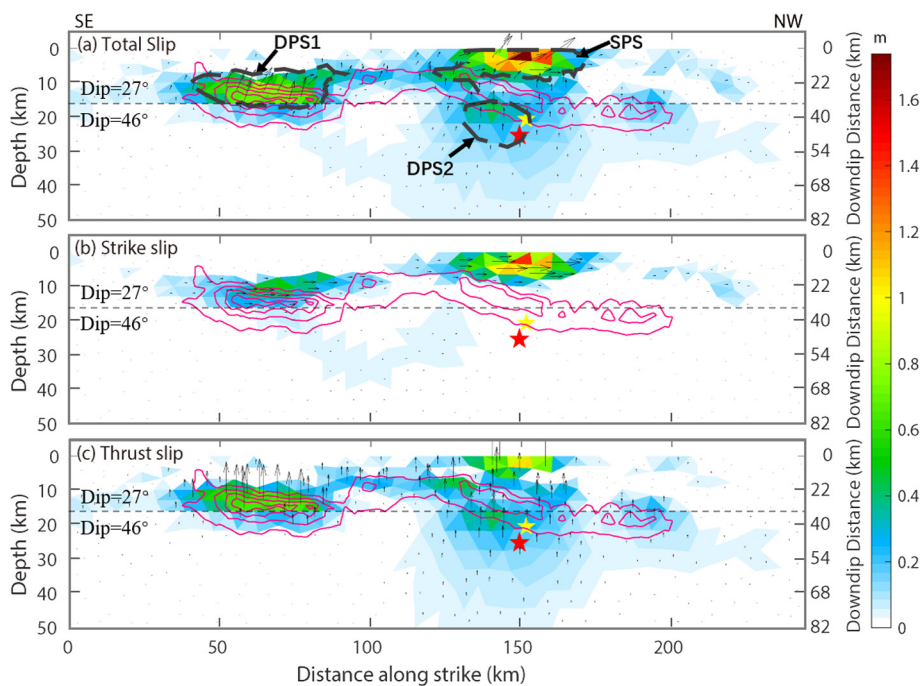


Figure 6. Results of distributed postseismic slip. (a) The total afterslip with black dashed polygons delineating the SPS, DPS1, and DPS2 zones. (b) and (c) show the strike and thrust slip components, respectively. The red and yellow stars represent the hypocenters of the 2018 Papua New Guinea (PNG) earthquake and largest M_w 6.7 aftershock, respectively. Smoothed 1 m contours of coseismic slip are shown in red. Arrows indicate the slip vector. Gray dashed lines are the 16-km transition depth separating shallow (27°) flat and deep ramp (46°) fault segments.

double-lobe (uplift and subsidence) displacement pattern in the case of 2015 M_w 7.8 Nepal earthquake (Elliott et al., 2016). The 2015 Nepal earthquake caused significant subsidence in the high Himalaya, which is characterized by interseismic uplift at about 4 mm/yr (Herman et al., 2010). However, given the dominant one-lobe uplift pattern related to the steep dip angles (shallow 27° and deep 46°), and the apparent correlation between the one-lobe uplift and topography in the 2018 PNG earthquake, we infer that coseismic uplift makes a significant contribution to the long-term permanent deformation in the PFB. Both coseismic and postseismic slip in this study likely contribute to the permanent deformation (Figure 5, Figures S2 and S3 in Supporting Information S1). However, the long-term permanent deformation needs to be studied further by continuous acquisitions of postseismic geodetic data for a long period.

3.3. Postseismic Slip Inversion

To determine whether both postseismic and coseismic slip occurred on the same fault, we applied the same inversion method and Monte Carlo approach to invert for the fault source parameters during the postseismic period spanning about 6 months starting only 1 day (ascending interferogram) and 5 days (descending interferogram) after the mainshock (Table 1). The estimated fault strike and dip angles are about 290° and 35° , respectively (Tables S1, S3, and Figure S8 in Supporting Information S1), which are close to those of the estimated coseismic fault. The estimated surface traces of the coseismic and postseismic model faults are very close to each other. Thus, considering the small differences in fault geometry, the overlapping fault traces, and inherent parameter uncertainties, we suggest that the postseismic fault slip occurred on the same fault hosting the coseismic rupture.

Our preferred distributed afterslip model shows three major postseismic slip zones. The shallow postseismic slip (SPS) zone extends from the surface to 10-km depth with a maximum slip of 1.7 m, located updip from the hypocenter and coseismic slip zone (Figure 6). A deeper postseismic slip (DPS1) zone is found at 7–20-km depth, overlapping with the peak-slip zone of the coseismic rupture. And another, even deeper postseismic slip (DPS2) zone is situated at 15–27-km depth near the USGS hypocenter and located below the SPS. It is worth noting that

the SPS shows a substantial component of left-lateral slip, but the DPS1 and DPS2 are dominated by thrust fault movement.

We estimated a postseismic moment release of 7.12×10^{19} Nm from the postseismic fault slip model, which is equivalent to M_w 7.17. This corresponds to $\sim 25\%$ of the coseismic moment release. We determined the ratio of moment released by afterslip and aftershocks within the three postseismic zones according to the $M_w > 4.0$ aftershocks reported by USGS for the same time period (Table S4 in Supporting Information S1). Overall, the estimated aseismic afterslip moment of 4.12×10^{19} Nm (M_w 7.08) is about 1.7 times that released by the recorded aftershocks (Table S4 in Supporting Information S1). The moment release in the SPS and DPS1 zones is characterized by a dominant contribution from aseismic afterslip with a ratio of 3.03 and 3.86, respectively. In addition, the aseismic afterslip contributes only 18% of the moment released in the DPS2 zone, primarily due to the largest M_w 6.7 aftershock (20.5 km).

The postseismic slip in SPS and DPS2 is mostly located updip and downdip of the coseismic rupture, respectively. This complementary spatial pattern suggests that postseismic slip is driven by coseismic static stress changes (Remy et al., 2016; Wallace et al., 2017). Considering that several large aftershocks ($\geq M_w$ 6) occurred in the postseismic slip area and the moment estimated from afterslip is larger than that of aftershocks (Figure 1 and Table S4 in Supporting Information S1), we suggest that most of the aftershocks are driven by surrounding aseismic afterslip (Avouac, 2015; Hsu et al., 2006; Liu & Xu, 2019). The predicted postseismic displacements from our preferred model (Figure 6) fit both ascending and descending InSAR observations well (Figure 3). The RMS misfits are 3.0 and 2.6 cm for the postseismic ascending data and descending data, respectively. The remaining residuals may be explained by residual atmospheric artifacts, secondary failures and nonplanar fault geometry, and other postseismic mechanisms which we did not explicitly consider in our modeling of the early deformation transients (e.g., poroelastic rebound and viscoelastic relaxation).

3.4. Uncertainty of Slip Distribution

In order to quantitatively assess the slip distribution, we determined the uncertainty level of the discrete slip values by perturbing our downsampled data 100 times with random Gaussian white noise (the noise level is determined by the standard deviations from covariances determined in the downsampled process (Figure S4 in Supporting Information S1; Liu & Xu, 2019)), which are then inverted to generate 100 perturbed slip distributions. The 1σ standard deviations of the slip distribution are calculated from these perturbed results (Figures S9 and S10 in Supporting Information S1). The estimated uncertainties are generally low for both coseismic slip ($1\sigma < 20$ cm) and postseismic slip ($1\sigma < 10$ cm) inversions. In addition, the resolution of the slip distribution is also determined to qualitatively assess the slip results (Barnhart & Lohman, 2010; Figures S11 and S12 in Supporting Information S1). While this analysis does not account for unmodeled factors, such as the effects of geometric complexity or heterogeneous elastic properties, we can conclude that all first-order features of the slip models are well resolved.

4. Discussion

4.1. Basement-Involved Thick-Skinned Structure in PNG Orogen

The dominant tectonic deformation style of the PFB (i.e., thin-skinned and/or thick-skinned) remains under dispute. The basement-involved thick-skinned scenario considers that the fold and thrust belt deformation reaches down into the crystalline basement, while the pure thin-skinned scenario argues that fault-fold deformation solely occurs in shallow thrust sheets where the deforming sedimentary cover is detached from the crystalline basement (Chapple, 1978; Pfiffner, 2017). Thus, one of the key criteria to distinguish thin-skinned and thick-skinned orogens lies in whether deformation due to faults in the crystalline basement significantly contributes to near-surface displacements (Craig & Warvakai, 2009).

The location of the 2018 PNG earthquake is consistent with having occurred on an active thrust fault referred to as Frontal Fault (Figure 1), although the exact location and name of the main frontal fault are variable in the published literature (e.g., Abers & McCaffrey, 1988; Koulali et al., 2015; Mahoney et al., 2021; Wallace et al., 2004). Our estimated coseismic rupture on a flat-ramp thrust fault reaches deep down into the crystalline basement to about 30-km depth, which is well below the depth (7–10 km) of the sedimentary cover (e.g., Hill et al., 2010; Mahoney

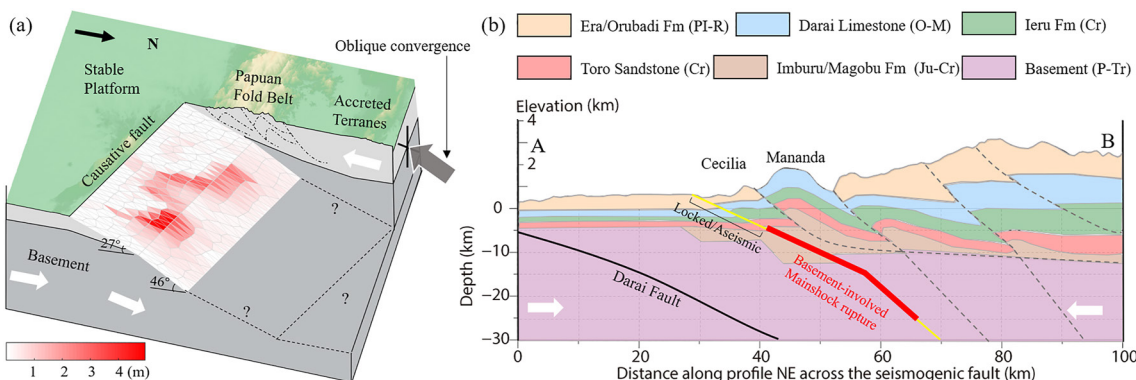


Figure 7. Schematic illustration of the seismogenic fault geometry of the 2018 Papua New Guinea (PNG) earthquake and geologic cross-section to illuminate the basement-involved fault rupture and earthquake-related fold growth. (a) Coseismic rupture on the resolved flat-ramp geometry (with the hangingwall block removed to reveal the slip zone). The deep flat/ramp structure (dashed lines) is poorly constrained. (b) Geologic SW-NE profile A–B (Figure 1) across the Mananda anticline modified from Mahoney et al. (2021).

et al., 2017, 2021), clearly indicating deep basement-involved deformation and accommodating thick-skinned style shortening in part via large earthquakes (Figures 4 and 7). Thus, the brittle crustal deformation during the 2018 PNG earthquake penetrates most of the crust, considering the average crustal thickness of 35 km in the PFB (Laske et al., 2013). Within this framework, we suggest that thick-skinned structures are currently active in the frontal PFB. This is also supported by the moment centroid depths (11–22 km) of other earthquakes deep below the sedimentary section in the PNG mountain belt reported by (Abers & McCaffrey, 1988) and the centroid depths (12–33 km) of historical earthquakes in the PFB with high-quality depth estimates (L1 events with depth error <5 km) catalogued by ISC-EHB (Figure S13 in Supporting Information S1). The differences in relocated depths by Engdahl et al. (1998) with the ISC-EHB estimates are generally small (0.3 km).

In addition, surface exposures of elevated crystalline basement also suggest that present-day tectonic activity is controlled by thick-skinned basement structures (Craig & Warvakai, 2009). In addition, thick-skinned deformation due to basement inversion of Mesozoic normal faults has been considered as one of the main reasons for many of the observed structures in the PFB (Buchanan & Warburton, 1996). Mahoney et al. (2021) note the reactivated inversion of the Komewu and Darai extensional basement faults on the northern Australian passive margin and propose that they share morphological and geometric similarities with the scale and pattern of ground displacement associated with the PNG earthquake. Moreover, granodioritic basement (K-Ar dated at 205 ± 5 Ma, P-Tr) was encountered by the well in the P'nyang gas field (Valenti, 1993). Seismic lines show that the northeast hinterland (hanging wall) is consistently elevated above the corresponding footwall blocks in the southwestern foreland, meaning that basement-involved deformation substantially contributes to the observed near-surface topography. This fits well with the thick-skinned structure deformation model (Figure 7) (Craig & Warvakai, 2009).

The positive relationship between mapped folds and their topographic expression and dominant vertical displacements during the PNG earthquake suggests a contribution of the fault slip on the Frontal Fault on the topography building and fold growth (Figure 5; Daout et al., 2021). Numerical models suggest that deformation only of shallow weak sedimentary cover cannot support the regional topography in the Zagros Mountain (Lacombe & Bellahsen, 2016), indicating that shortening associated with thick-skinned structures has a significant role in the topography building. Thus, the likely scenario for driving the frontal uplift in the PFB is a contribution of thick-skinned deformation via large earthquakes, which probably involves tectonic inversion of an earlier extensional fault system beneath the PFB (Mahoney et al., 2021). Fault-related folds represent a significant deformation in compressional regimes (i.e., fold and thrust belts) (Brandes & Tanner, 2014). Numerical simulations suggest that fault bends (e.g., flat-ramp fault geometry) lead to contemporaneous faulting and folding in the upper plate (Mallick et al., 2021; Sathiakumar et al., 2020). The residual interferograms (Figures 2 and 3 and Figures S1 and S2 in Supporting Information S1), show clear unmodeled residual LOS signal that coincides spatially with some anticlinal ranges, which can be explained by structural growth controlled by faulting propagations during earthquakes (Hanani et al., 2016). For instance, in the Lavani Range, ~15 cm localized LOS uplift can be observed in both ascending and descending residuals (Figures 2c and 2f), which cannot be explained by residual atmospheric artifacts (Figure S1 in Supporting Information S1). Significant LOS residuals can also be recognized

near the Hides, Angore, Mananda, Moran, and Agogo anticlines, which host the main gas/oil resources in PNG. Several anticlines in the frontal PFB have been interpreted as manifestations of primarily deeply rooted and thick-skinned deformation, including the Juha Anticline (Hanani et al., 2016; Smith, 1990) and the Cecilia Anticline (Cole et al., 2000). This suggests that thick-skinned ruptures, including the 2018 PNG earthquake, play an important role in the deformation, erosion, and deposition of shallow sediments of the frontal fold and thrust belt, and indicates current active fold growth of the PFB (Hamilton, 1979; Wallace et al., 2004). Fold growth caused by faulting during earthquakes has also been proposed in other regions based on geodetic observations (Belabbès et al., 2009; Nissen et al., 2007; Pezzo et al., 2013; Stein & King, 1984; Tizzani et al., 2013). Considering our geodetic evidence of basement-involved thick-skinned deformation and flat-ramp fault geometry, we suggest that the topography/fold growth during the PNG earthquake is likely dominated by the underlying thick-skinned rupture (Madrtsch et al., 2008). However, the SPS suggests the activation of short-term thin-skinned processes during the postseismic period, indicating interaction between thick-skinned and thin-skinned deformation. This is consistent with the stress loading in the shallow crust (Figure S14 in Supporting Information S1) induced by the thick-skinned coseismic rupture.

A nearly universal assumption is that slip on underlying causative faults dominates crustal-scale fold growth, however, off-fault deformation especially in the shallow sedimentary cover is a significant component of fold growth (Johnson, 2018; Mallick et al., 2021; Sathiakumar et al., 2020). Boundary element models of fault-related folding with viscoelastic layers suggest that fold growth involves distributed off-fault deformation and bedding plane slip (Johnson, 2018). Stress perturbation caused by slip of active faults will promote fold growth especially within thick sedimentary cover (Johnson, 2018; Ramsey et al., 2008). The stress change in the shallow sedimentary cover induced by slip on the causative faults during the 2018 PNG earthquake (Figure S14 in Supporting Information S1), shows apparent positive stress perturbation at the locations of several anticlines (e.g., Juha, Lavani, Angore, Mananda, Agogo). This indicates the fold growth during the PNG earthquake also involved distributed off-fault deformation, which is supported by numerical simulation framework that combines an elastoplastic model of folding with a rate-state frictional model of fault strength in a layered medium (Mallick et al., 2021). However, due to the mechanical coupling between elastic coseismic slip and off-fault deformation (i.e., fold growth), it is difficult to distinguish quantitatively the folding-related contribution during large earthquake, which should be considered in the fault kinematics inversion and deserves further study to illustrate more realistic earthquake deformation processes in fold and thrust belts. Numerical modeling of short-term and long-term deformation with elastoplastic rheologies, using the finite element method, is one approach to tackle this kind of coupled problem (e.g., Baden et al., 2022).

4.2. Variable Coseismic and Postseismic Slip Behaviors

We observe that the distribution of coseismic slip is characterized by dominant thrust slip (Figure 4), while the postseismic slip is mainly confined to three separate regions at different depths with different dominant strike/thrust slip patterns (Figure 6). The coseismic and postseismic slip areas appear spatially overlapped in the DPS1 zone, but not in the SPS and DPS2 zones (Figure 6), where both seismic and aseismic slip behaviors are observed (Table S4 in Supporting Information S1). Postseismic slip model with the constraint of no slip in zones of large coseismic slip (>0.5 m), show much larger residuals than for the model with no constraint (Figure S15 in Supporting Information S1), suggest the reasonability of the overlapped coseismic and postseismic slip. The shallow part of reverse faults is often described as having velocity-strengthening frictional properties, e.g. (Marone, 1998), due to the presence of unconsolidated sediments, which generally impedes the coseismic rupture propagation and favors aseismic slip, e.g. (Brooks et al., 2017; Wang & Bürgmann, 2020). The observed complicated slip behaviors suggest that there exists strong spatial heterogeneity of fault frictional properties on the fault hosting the PNG earthquake (Qiu et al., 2019). The coexistence of seismic and aseismic slip in the SPS and DPS1 zones indicates that either the frictional behavior is neutral with the rate-state frictional parameter $a-b$ near zero allowing for transitional fault behavior (Liu & Xu, 2019) or that complex and variable ambient conditions (e.g., fluid pressure and material heterogeneity) allow for dynamic weakening mechanisms (Noda & Lapusta, 2013; Perfettini & Avouac, 2014; Qiu et al., 2019). Experimental results suggest that fault gouge can transition from velocity-strengthening to velocity-weakening behavior under certain conditions of displacement and induration, which may explain the mixed slip behavior (Biegel et al., 1989; Roesner et al., 2020).

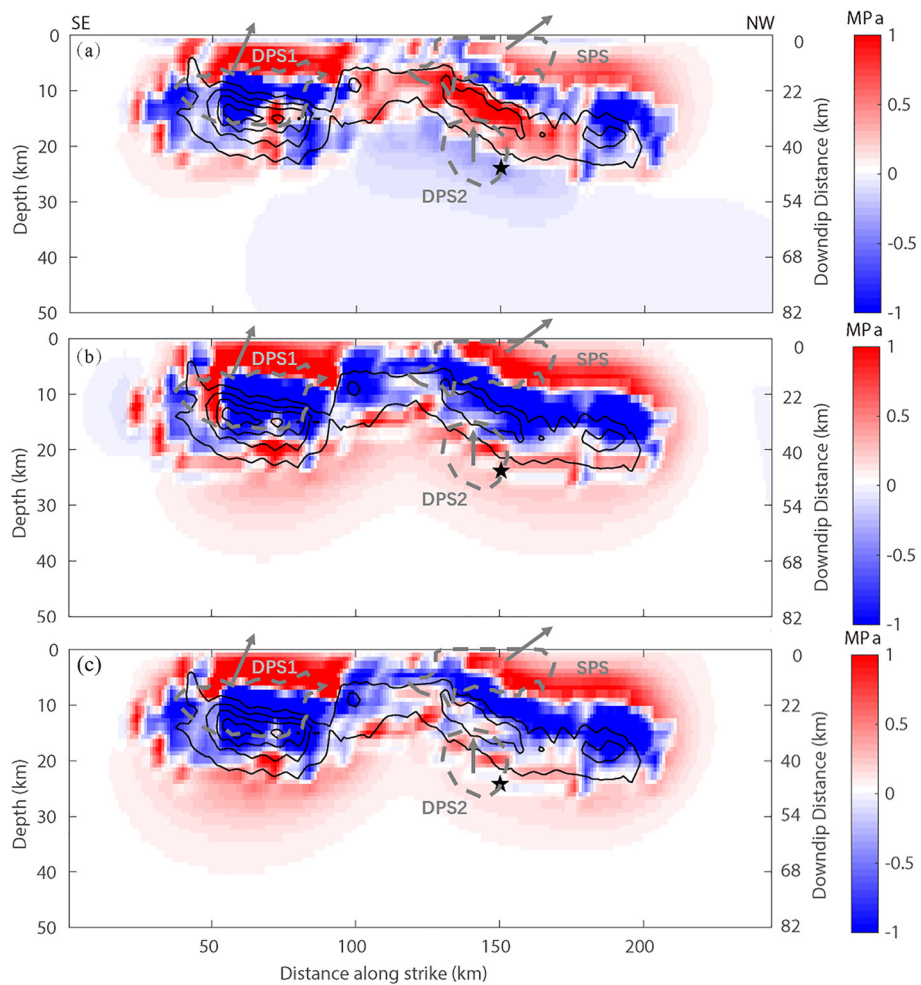


Figure 8. Coulomb stress change on fault plane (Figure 1) caused by 2018 Papua New Guinea (PNG) earthquake calculated with the estimated coseismic slip model. Note that the rake angle of the receiver fault is set as (a) 0° (encouraging left-lateral strike-slip), (b) 90° (encouraging thrust slip), and (c) 44° (encouraging oblique slip). Gray dashed polygons and arrows indicate the corresponding SPS/DPS1/DPS2 zones and mean postseismic slip rake directions in SPS/DPS1/DPS2, respectively (Figure 6a). Black smoothed 0.5 m contours and star represent coseismic slip and USGS hypocenter.

The shallow postseismic oblique slip observed in the SPS zone may be partially associated with the horizontal shear-stress changes induced by the 2018 PNG earthquake. To test if the inferred strike-slip component represents afterslip driven by the coseismic rupture, we calculated the mainshock-induced coulomb stress change $\Delta CFS = \Delta\tau + \mu'\Delta\sigma$ with the estimated coseismic slip (Figure 8), assuming an effective friction coefficient of $\mu' = 0.4$ on the receiver fault (Lin & Stein, 2004). Here, $\Delta\tau$ is shear-stress change (Figure S16 in Supporting Information S1, positive when sheared in the rake direction) and $\Delta\sigma$ is normal stress change (Figure S17 in Supporting Information S1, positive if the fault is unclamped). The maximum Coulomb stress change in the along-strike direction caused by the PNG mainshock is about 0.2 MPa in the SPS zone (Figure 8a), which is far less than the stress changes encouraging thrusting (Figure 8b) and the calculated static postseismic horizontal stress drop of ~ 3.5 MPa (Ripperger & Mai, 2004). This implies the postseismic strike-dominant slip in the SPS zone was a triggered episode involving both seismic and aseismic release of long-term stress build up. In addition, the moment released in the DPS2 zone is dominated by thrust slip indicates the coseismic stress perturbation induced the moment release in the DPS2 zone (Figure 8). This is confirmed by the coseismic Coulomb stress changes mostly encouraging thrusting (Figure 8b, dominating by shear-stress change (Figures S16b and S17b in Supporting Information S1)) but inhibiting sinistral slip (Figure 8a, dominating by normal stress change (Figures S16a and S17a in Supporting Information S1)) in the DPS2 zone.

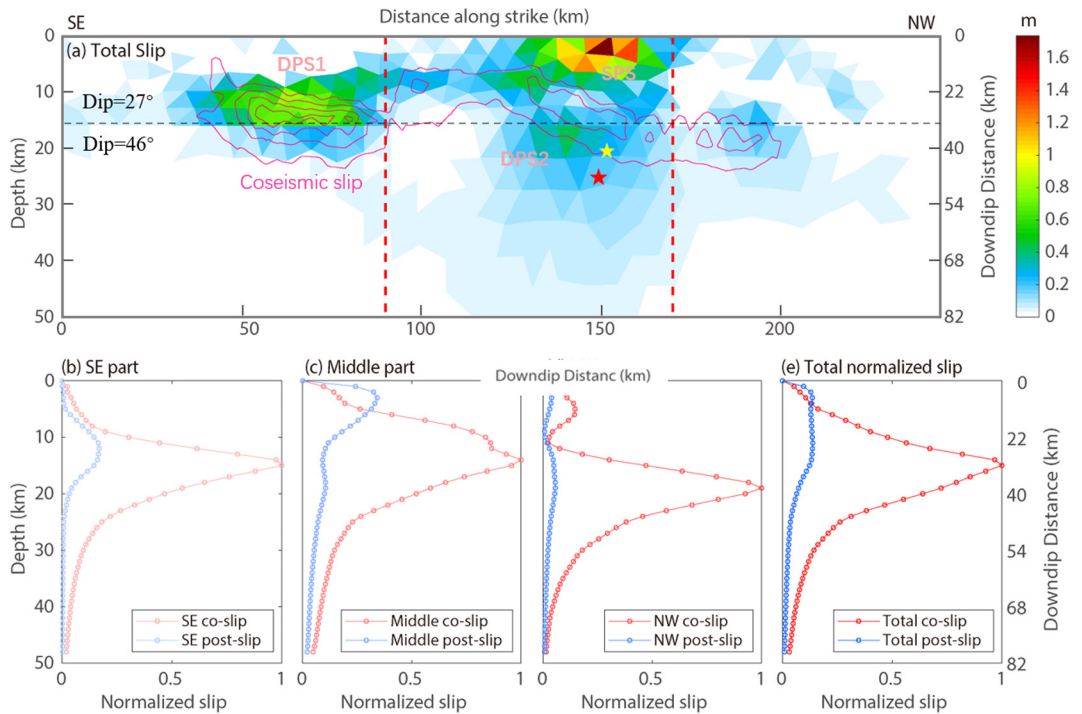


Figure 9. Normalized fault slip as a function of depth. (a) Postseismic slip with coseismic slip indicated by 1-m interval red contours, and red dashed line divides the slip model into South-East (SE), middle, and North-West (NW) parts. The gray dashed line is the 16 km transition depth separating the shallow flat (27°) and deep ramp (46°) fault segments. (b), (c), and (d) show the comparation between normalized coseismic and postseismic slip in SE, middle, and NW parts, respectively. (e) The total normalized slip comparation.

Strain partitioning is well documented along oblique convergent tectonic boundaries (Loveless & Meade, 2010; McCaffrey, 1992; Seeber & Pêcher, 1998), involving the accommodation of oblique convergence by separate strike-slip and thrust fault structures (Seeber & Pêcher, 1998). Our coseismic slip model shows that the fault rupture is dominated by thrust slip with a minor, left-lateral strike-slip component near the DPS1 zone (Figure 4). The postseismic slip shows similar dominant dip-slip with an average rake angle of 66° for the slip patches (>0.3 m) in the DPS1 zone, indicating the postseismic slip kinematics is similar to that of the coseismic slip. In contrast, the postseismic slip (>0.3 m) has an average rake angle of 44° (strike-slip-dominated) and 90° (pure thrust slip) in the SPS and DPS2 zones, respectively. The layered slip behaviors with depth support partitioning of deformation between deep inherited basement fault structures and shallow fold-thrust structures in the sedimentary cover (Figures 7 and 9; Allen et al., 2017). We also calculate the moment-release ratio between strike-slip and thrust slip for both coseismic (23%) and postseismic (67%) slip models (Figures 4 and 6). The strike-slip moment-release ratio in the postseismic observation period is much higher than the coseismic one, indicating more obvious slip partitioning and that the strike-slip component of plate motion may be largely accommodated during postseismic slip. It, however, will take decades or even centuries of geodetic data to validate whether this phenomenon persists over a longer period.

4.3. Shallow Slip Deficit and Seismic Hazard

A SSD, that is a pronounced reduction or lack of coseismic slip in the uppermost crust, has been quite commonly observed for different strike-slip (Fialko et al., 2005; Liu, Xu, He, et al., 2022; Xu et al., 2016), normal faulting (Liu, Xu, Radziminovich, et al., 2022; Xu et al., 2019), and reverse faulting earthquakes (Liu & Xu, 2019; Wang & Fialko, 2015). A better understanding of the nature of the SSD is important for improved understanding of seismic hazard and crustal rheology. One possible explanation of the SSD suggests that the uppermost few kilometers of the brittle crust impede the coseismic rupture propagation according to the rate-and-state law (Liu & Xu, 2019; Marone et al., 1991). The rate-and-state law describes stable velocity strengthening regions with positive $a-b$ value preferring aseismic slip and unstable velocity-weakening regions with negative $a-b$ value preferring seismic

slip (nucleation) or slow slip events with low slip values. This implies that the SSD can be compensated by afterslip and/or shallow interseismic creep (Marone et al., 1991; Scholz, 2019). Poorly consolidated shallow sediments combined with low fault-normal stress also favor the likelihood of more distributed cataclastic deformation in the shallow crust (Brooks et al., 2017; Fialko et al., 2005; Kaneko & Fialko, 2011). Fialko et al. (2005) suggested that the origin of the SSD can be attributed to inelastic deformation in the uppermost crust including young and developing faults, which is not considered in elastic slip models. Kaneko and Fialko (2011) also suggest a maximum SSD of 15% can be explained by inelastic deformation in the model scenarios they considered.

In addition, limited data coverage near the surface rupture of strike-slip earthquakes (1992 Landers, 1999 Hector Mine, etc.) can lead to underestimated shallow slip (Xu et al., 2016, and references therein). However, with data near the fault trace (Figure 2a and Figure S1a in Supporting Information S1), our model results still show an obvious SSD for the PNG thrust earthquake (Figure 9), which is consistent with the coseismic results from pixel offset observations showing shallow SSD (Chong & Huang, 2020). This suggests that a lack of near-fault-trace data has much less impact on SSD for thrust earthquakes not breaking to the surface than that for strike-slip earthquakes breaking to the surface.

An obvious SSD is found in the top ~5 km of the shallow crust during the PNG earthquake (Figures 4 and 6). The postseismic slip can account for ~35% of the SSD if only the middle part of the fault hosting the SPS is considered (Figure 9c), while the southeastern and northeastern parts show no obvious postseismic SSD compensation (Figures 9b and 9d). This discrepancy may be explained by the existence of thick sedimentary units near the SPS, with a different lithology from the adjacent sections of the rupture (Mahoney et al., 2021). In total, postseismic slip associated with afterslip and aftershocks compensates only about 15% of the SSD (Figure 9d). It should be noted that the postseismic interferogram does not capture the signal of the first day after the mainshock due to the limited revisiting period of the SAR satellite, which may lead to the underestimation of postseismic slip. However, the missing very early postseismic phase is far from enough to make up the large SSD.

Our results suggest that prevalent inelastic deformation and/or future large shallow earthquakes on the same or nearby faults are required to compensate the observed SSD. Folding is widely distributed in the PNG orogen belts, and we see evidence of localized fold growth in our residual deformation maps (Figures 2 and 3). This may be the dominant mechanism of permanent inelastic deformation in the PFB (Hanani et al., 2016), and upper crustal folding likely plays an important role in accommodating the convergence between the Pacific and Australian plates. However, inelastic fold growth is mainly concentrated in the coseismic surface displacement zone (Figures 2 and 3), and thus provides little compensation for the observed SSD in the PNG earthquake. Unless substantial shallow fold growth also occurs interseismically, the existence of a large SSD may indicate that the shallow part of the fault remains locked. Therefore, the occurrence of a future large shallow earthquake on the PNG seismogenic fault or other thrusts accommodating the convergence in the shallower sedimentary section (e.g., fold-thrust deformation) could be possible.

5. Conclusions

In this study, we generate both coseismic and postseismic displacement fields covering the 2018 PNG earthquake using InSAR data. We find that the InSAR observations can be well explained by fault slip on one flat-ramp seismogenic fault dipping northeastward beneath the PFB, with a strike angle of 297°, a shallow dip angle of 27° and deep dip angle of 46°. Coseismic slip is dominated by fault thrust slip with a peak value of 4.9 m, and postseismic slip is mainly located in two separate deep postseismic slip (DPS) and one SPS zones. The fault slip models suggest that coseismic slip ruptured down to 30 km in the crystalline basement implying that active thick-skinned structures exist beneath the PFB and play an important role in the current PNG frontal orogen evolution. Complex fault slip patterns, including the coexistence of seismic and aseismic slip behaviors in the SPS zone and the overlapped coseismic and postseismic slip in the DPS zone, indicate remarkable heterogeneity in fault frictional properties. Distinct shallow and deep fault slip patterns, and deep inherited basement deformation and shallow fold-thrust deformation in the sedimentary cover confirm that stress-strain partitioning exists in the oblique collision PNG orogen. The observed SSD was not fully compensated by postseismic slip and off-fault inelastic deformation during the observation period, indicating that the occurrence of future shallow earthquakes in the area cannot be ruled out.

Data Availability Statement

ALOS-2 SAR images are provided by the Japan Aerospace Exploration Agency (No. ER3A2N521). The GAMMA commercial software is obtained from <https://www.gamma-rs.ch/software>. The Coulomb3 software is available from <https://www.usgs.gov/software/coulomb-3>. The Generic Mapping Tools created figures are obtained from <https://www.genericmapping-tools.org/>. Regional faults are obtained from <http://databank.igl.earthquake.cn/map/ActiveFault/introFault.html>. The seismicity catalog used in this work is openly available at the United States Geological Survey (<https://earthquake.usgs.gov/earthquakes/search/>) and International Seismological Centre (<http://www.isc.ac.uk/iscbulletin/search/fmechanisms/interactive/>). Several figures were prepared using the Generic Mapping Tools software (Wessel et al., 2019). The processed data used in the study are available (<http://doi.org/10.5281/zenodo.6596540>).

Acknowledgments

We thank Editor Isabelle Manighetti, Associate Editor and two anonymous reviewers for their constructive reviews and comments. We would like to thank to Jean-Philippe Avouac for his valuable suggestions and communications during the development of this work. This work was supported by the National Natural Science Foundation of China (No. 42174023), by the Innovation Foundation for Postgraduate of Central South University (No. 2020zzts181), and by the Hunan Provincial Innovation Foundation for Postgraduate (No. CX20200344).

References

- Abers, G., & McCaffrey, R. (1988). Active deformation in the New Guinea fold-and-thrust belt: Seismological evidence for strike-slip faulting and basement-involved thrusting. *Journal of Geophysical Research*, 93, 13332–13354. <https://doi.org/10.1029/jb093ib11p13332>
- Allen, M. B., Walters, R. J., Song, S. G., Saville, C., De Paola, N., Ford, J., et al. (2017). Partitioning of oblique convergence coupled to the fault locking behavior of fold-and-thrust belts: Evidence from the Qilian Shan, northeastern Tibetan Plateau. *Tectonics*, 36, 1679–1698. <https://doi.org/10.1002/2017TC004476>
- Avouac, J. P. (2015). From geodetic imaging of seismic and aseismic fault slip to dynamic modeling of the seismic cycle. *Annual Review of Earth and Planetary Sciences*, 43, 233–271. <https://doi.org/10.1146/annurev-earth-060614-105302>
- Baden, C. W., Shuster, D. L., Aron, F., Fosdick, J. C., Burgmann, R., & Hiley, G. E. (2022). Bridging earthquakes and mountain building in the Santa Cruz Mountains, CA. *Science Advances*, 8, eabi6031. <https://doi.org/10.1126/sciadv.abi6031>
- Baldwin, S. L., Fitzgerald, P. G., & Webb, L. E. (2012). Tectonics of the New Guinea Region. *Annual Review of Earth and Planetary Sciences*, 40, 495–520. <https://doi.org/10.1146/annurev-earth-040809-152540>
- Barnhart, W., & Lohman, R. (2010). Automated fault model discretization for inversions for coseismic slip distributions. *Journal of Geophysical Research*, 115, B10419. <https://doi.org/10.1029/2010JB007545>
- Barnhart, W. D., Brengman, C. M. J., Li, S., & Peterson, K. E. (2018). Ramp-flat basement structures of the Zagros Mountains inferred from co-seismic slip and afterslip of the 2017 M w 7.3 Darbandikhan, Iran/Iraq earthquake. *Earth and Planetary Science Letters*, 496, 96–107. <https://doi.org/10.1016/j.epsl.2018.05.036>
- Belabbès, S., Meghraoui, M., Çakir, Z., & Bouhadad, Y. (2009). InSAR analysis of a blind thrust rupture and related active folding: The 1999 Ain Temouchent earthquake (Mw 5.7, Algeria) case study. *Journal of Seismology*, 13, 421–432.
- Biegel, R. L., Sammis, C. G., & Dieterich, J. H. (1989). The frictional properties of a simulated gouge having a fractal particle distribution. *Journal of Structural Geology*, 11, 827–846. [https://doi.org/10.1016/0191-8141\(89\)90101-6](https://doi.org/10.1016/0191-8141(89)90101-6)
- Brandes, C., & Tanner, D. C. (2014). Fault-related folding: A review of kinematic models and their application. *Earth-Science Reviews*, 138, 352–370. <https://doi.org/10.1016/j.earscirev.2014.06.008>
- Brooks, B. A., Minson, S. E., Glennie, C. L., Nevitt, J. M., Dawson, T., Rubin, R., et al. (2017). Buried shallow fault slip from the South Napa earthquake revealed by near-field geodesy. *Science Advances*, 3, e1700525. <https://doi.org/10.1126/sciadv.1700525>
- Buchanan, P. G., & Warburton, J. (1996). The influence of pre-existing basin architecture in the development of the Papuan fold and thrust belt: Implications for petroleum prospective. Papua New Guinea (PNG) Petroleum Convention Proceedings.
- Chapple, W. M. (1978). Mechanics of thin-skinned fold-and-thrust belts. *Geological Society of America Bulletin*, 89, 1189–1198. [https://doi.org/10.1130/0016-7606\(1978\)89<1189:motfb>2.0.co;2](https://doi.org/10.1130/0016-7606(1978)89<1189:motfb>2.0.co;2)
- Chen, C. W., & Zebker, H. A. (2001). Two-dimensional phase unwrapping with use of statistical models for cost functions in nonlinear optimization. *Journal of the Optical Society of America A*, 18, 338–351. <https://doi.org/10.1364/josaa.18.000338>
- Chong, J.-H., & Huang, M.-H. (2020). Refining the 2018 Mw 7.5 Papua New Guinea earthquake fault-slip model using subpixel offset. *Bulletin of the Seismological Society of America*, 111, 1032–1042. <https://doi.org/10.1785/0120200250>
- Cole, J., Parish, M., & Schmidt, D. (2000). Sub-thrust plays in the Papuan fold belt: The next generation of exploration targets. Papua New Guinea (PNG) Petroleum Convention Proceedings.
- Craig, M. S., & Warvakai, K. (2009). Structure of an active foreland fold and thrust belt, Papua New Guinea. *Australian Journal of Earth Sciences*, 56, 719–738. <https://doi.org/10.1080/08120090903005360>
- Daout, S., Parsons, B., & Walker, R. (2021). Post-earthquake fold growth imaged in the Qaidam Basin, China, with Interferometric Synthetic Aperture Radar. *Journal of Geophysical Research: Solid Earth*, 126, e2020JB021241. <https://doi.org/10.1029/2020JB021241>
- Elliott, J. R., Jolivet, R., Gonzalez, P. J., Avouac, J. P., Hollingsworth, J., Searle, M. P., & Stevens, V. L. (2016). Himalayan megathrust geometry and relation to topography revealed by the Gorkha earthquake. *Nature Geoscience*, 9, 174–180. <https://doi.org/10.1038/ngeo2623>
- Engdahl, E. R., van der Hilst, R., & Buland, R. (1998). Global teleseismic earthquake relocation with improved travel times and procedures for depth determination. *Bulletin of the Seismological Society of America*, 88, 722–743.
- Farr, T. G., Rosen, P. A., Caro, E., Crippen, R., Duren, R., Hensley, S., et al. (2007). The Shuttle Radar Topography Mission. *Reviews of Geophysics*, 45, RG2004. <https://doi.org/10.1029/2005RG000183>
- Feng, W., & Li, Z. (2010). A novel hybrid PSO/simplex algorithm for determining earthquake source parameters using InSAR observations. *Progress in Geophysics*, 25, 1189–1196.
- Fialko, Y., Sandwell, D., Simons, M., & Rosen, P. (2005). Three-dimensional deformation caused by the Bam, Iran, earthquake and the origin of shallow slip deficit. *Nature*, 435, 295–299. <https://doi.org/10.1038/nature03425>
- Hamilton, W. B. (1979). Tectonics of the Indonesian region. US Government Printing Office. <https://doi.org/10.3133/pp1078>
- Hanani, A., Lennox, P., & Hill, K. (2016). The geology and structural style of the Juha gas field, Papua New Guinea. ASEG Extended Abstracts. 2016, 1–7. <https://doi.org/10.1071/aseg2016ab272>
- Herman, F., Copeland, P., Avouac, J.-P., Bollinger, L., Mahéo, G., Le Fort, P., et al. (2010). Exhumation, crustal deformation, and thermal structure of the Nepal Himalaya derived from the inversion of thermochronological and thermobarometric data and modeling of the topography. *Journal of Geophysical Research*, 115, B06407. <https://doi.org/10.1029/2008JB006126>

- Hill, K. C., Lucas, K., & Brady, K. (2010). Structural styles in the Papuan Fold Belt, Papua New Guinea: Constraints from analogue modelling. *Geological Society, London, Special Publications*, 348, 33–56. <https://doi.org/10.1144/sp348.3>
- Hobson, D. (1986). A thin skinned model for the Papuan thrust belt and some implications for hydrocarbon exploration. *The APPEA Journal*, 26, 214–225. <https://doi.org/10.1071/aj85021>
- Hsu, Y. J., Simons, M., Avouac, J. P., Galetzka, J., Sieh, K., Chlieh, M., et al. (2006). Frictional afterslip following the 2005 Nias-Simeulue earthquake, Sumatra. *Science*, 312, 1921–1926. <https://doi.org/10.1126/science.1126960>
- Hu, J., Li, Z. W., Ding, X. L., Zhu, J. J., Zhang, L., & Sun, Q. (2014). Resolving three-dimensional surface displacements from InSAR measurements: A review. *Earth-Science Reviews*, 133, 1–17. <https://doi.org/10.1016/j.earscirev.2014.02.005>
- Johnson, K. M. (2018). Growth of fault-cored anticlines by flexural slip folding: Analysis by boundary element modeling. *Journal of Geophysical Research: Solid Earth*, 123, 2426–2447. <https://doi.org/10.1002/2017JB014867>
- Jónsson, S., Zebker, H., Segall, P., & Amelung, F. (2002). Fault slip distribution of the 1999 M w 7.1 Hector Mine, California, earthquake, estimated from satellite radar and GPS measurements. *Bulletin of the Seismological Society of America*, 92, 1377–1389.
- Kaneko, Y., & Fialko, Y. (2011). Shallow slip deficit due to large strike-slip earthquakes in dynamic rupture simulations with elasto-plastic off-fault response. *Geophysical Journal International*, 186, 1389–1403. <https://doi.org/10.1111/j.1365-246x.2011.05117.x>
- Koulali, A., Tregoning, P., McClusky, S., Stanaway, R., Wallace, L., & Lister, G. (2015). New Insights into the present-day kinematics of the central and western Papua New Guinea from GPS. *Geophysical Journal International*, 202, 993–1004. <https://doi.org/10.1093/gji/ggv200>
- Lacombe, O., & Bellahsen, N. (2016). Thick-skinned tectonics and basement-involved fold-thrust belts: Insights from selected Cenozoic orogens. *Geological Magazine*, 153, 763–810. <https://doi.org/10.1017/s0016756816000078>
- Laske, G., Masters, G., Ma, Z., & Pasyanos, M. (2013). Update on CRUST1.0—A 1-degree global model of Earth's crust. *Geophysical Research Abstracts*, 26, 58.
- Li, Z. W., Ding, X. L., Huang, C., Zhu, J. J., & Chen, Y. L. (2008). Improved filtering parameter determination for the Goldstein radar interferogram filter. *ISPRS Journal of Photogrammetry and Remote Sensing*, 63, 621–634. <https://doi.org/10.1016/j.isprsjprs.2008.03.001>
- Lin, J., & Stein, R. S. (2004). Stress triggering in thrust and subduction earthquakes and stress interaction between the southern San Andreas and nearby thrust and strike-slip faults. *Journal of Geophysical Research*, 109, B02303. <https://doi.org/10.1029/2003JB002607>
- Liu, X., & Xu, W. (2019). Logarithmic model joint inversion method for coseismic and postseismic slip: Application to the 2017 Mw 7.3 Sarpol Zahab earthquake, Iran. *Journal of Geophysical Research: Solid Earth*, 124, 12034–12052. <https://doi.org/10.1029/2019JB017953>
- Liu, X., Xu, W., He, Z., Fang, L., & Chen, Z. (2022). Aseismic Slip and Cascade Triggering Process of Foreshocks Leading to the 2021 M w 6.1 Yangbi Earthquake. *Seismological Research Letters*, 93(3), 1413–1428. <https://doi.org/10.1785/0220210263>
- Liu, X., Xu, W., Radziminovich, N. A., Fang, N., & Xie, L. (2022). Transtensional coseismic fault slip of the 2021 Mw 6.7 Turt Earthquake and heterogeneous tectonic stress surrounding the Hovsgol Basin, Northwest Mongolia. *Tectonophysics*, 229407. <https://doi.org/10.1016/j.tecto.2022.229407>
- Loveless, J. P., & Meade, B. J. (2010). Geodetic imaging of plate motions, slip rates, and partitioning of deformation in Japan. *Journal of Geophysical Research*, 115, B02410. <https://doi.org/10.1029/2008JB006248>
- Madritsch, H., Schmid, S. M., & Fabbri, O. (2008). Interactions between thin- and thick-skinned tectonics at the northwestern front of the Jura fold-and-thrust belt (eastern France). *Tectonics*, 27, TC5005. <https://doi.org/10.1029/2008TC002282>
- Mahoney, L., Hill, K., McLaren, S., & Hanani, A. (2017). Complex fold and thrust belt structural styles: Examples from the Greater Juha area of the Papuan fold and thrust belt, Papua New Guinea. *Journal of Structural Geology*, 100, 98–119. <https://doi.org/10.1016/j.jsg.2017.05.010>
- Mahoney, L., Stanaway, R., McLaren, S., Hill, K., & Bergman, E. (2021). The 2018 Mw 7.5 highlands earthquake in Papua New Guinea: Implications for structural style in an active fold and thrust belt. *Tectonics*, 40, e2020TC006667. <https://doi.org/10.1029/2020TC006667>
- Mallick, R., Bürgmann, R., Johnson, K., & Hubbard, J. (2021). A unified framework for earthquake sequences and the growth of geological structure in fold-thrust belts. *Journal of Geophysical Research: Solid Earth*, 126, e2021JB022045. <https://doi.org/10.1029/2021JB022045>
- Manighetti, I., Campillo, M., Bouley, S., & Cotton, F. (2007). Earthquake scaling, fault segmentation, and structural maturity. *Earth and Planetary Science Letters*, 253, 429–438. <https://doi.org/10.1016/j.epsl.2006.11.004>
- Manighetti, I., Mercier, A., & De Barros, L. (2021). Fault trace corrugation and segmentation as a measure of fault structural maturity. *Geophysical Research Letters*, 48, e2021GL095372. <https://doi.org/10.1029/2021GL095372>
- Marone, C. (1998). Laboratory-derived friction laws and their application to seismic faulting. *Annual Review of Earth and Planetary Sciences*, 26, 643–696. <https://doi.org/10.1146/annurev.earth.26.1.643>
- Marone, C. J., Scholtz, C. H., & Bilham, R. (1991). On the mechanics of earthquake afterslip. *Journal of Geophysical Research*, 96, 8441–8452. <https://doi.org/10.1029/91JB00275>
- Mason, R. (1997). Structure of the Alice anticline, Papua New Guinea: Serial balanced cross-sections and their restoration. *Journal of Structural Geology*, 19, 719–734. [https://doi.org/10.1016/s0191-8141\(96\)00114-9](https://doi.org/10.1016/s0191-8141(96)00114-9)
- McCaffrey, R. (1992). Oblique plate convergence, slip vectors, and forearc deformation. *Journal of Geophysical Research*, 97, 8905–8915. <https://doi.org/10.1029/92JB00483>
- Nissen, E., Ghorashi, M., Jackson, J., Parsons, B., & Talebian, M. (2007). The 2005 Qeshm Island earthquake (Iran)—A link between buried reverse faulting and surface folding in the Zagros Simply Folded Belt? *Geophysical Journal International*, 171, 326–338. <https://doi.org/10.1111/j.1365-246x.2007.03514.x>
- Noda, H., & Lapusta, N. (2013). Stable creeping fault segments can become destructive as a result of dynamic weakening. *Nature*, 493, 518–521. <https://doi.org/10.1038/nature11703>
- Okada, Y. (1985). Surface deformation due to shear and tensile faults in a half-space. *Bulletin of the Seismological Society of America*, 75, 1135–1154. <https://doi.org/10.1785/bssa0750041135>
- Ollarves, R., Zhao, S., & Gilby, F. (2020). Interaction between the folded structures of the Western Papua New Guinea Highlands: An example of how surface observations can assist in subsurface understanding. *Geological Society, London, Special Publications*, 490, 311–327. <https://doi.org/10.10144/sp490-2018-124>
- Perfettini, H., & Avouac, J. P. (2014). The seismic cycle in the area of the 2011 Mw 9.0 Tohoku-Oki earthquake. *Journal of Geophysical Research: Solid Earth*, 119, 4469–4515. <https://doi.org/10.1002/2013JB010697>
- Pezzo, G., Merryman Boncori, J. P., Tolomei, C., Salvi, S., Atzori, S., Antonioli, A., et al. (2013). Coseismic deformation and source modeling of the May 2012 Emilia (Northern Italy) earthquakes. *Seismological Research Letters*, 84, 645–655. <https://doi.org/10.1785/0220120171>
- Pfiffner, O. A. (2017). Thick-skinned and thin-skinned tectonics: A global perspective. *Geosciences*, 7, 71. <https://doi.org/10.3390/geosciences7030071>
- Qiu, Q., Feng, L., Hermawan, I., & Hill, E. M. (2019). Coseismic and postseismic slip of the 2005 Mw 8.6 Nias-Simeulue earthquake: Spatial overlap and localized viscoelastic flow. *Journal of Geophysical Research: Solid Earth*, 124, 7445–7460. <https://doi.org/10.1029/2018JB017263>

- Ramsey, L. A., Walker, R. T., & Jackson, J. (2008). Fold evolution and drainage development in the Zagros Mountains of Fars province, SE Iran. *Basin Research*, 20, 23–48. <https://doi.org/10.1111/j.1365-2117.2007.00342.x>
- Remy, D., Perfettini, H., Cotte, N., Avouac, J. P., Chlieh, M., Bondoux, F., et al. (2016). Postseismic relocking of the subduction megathrust following the 2007 Pisco, Peru, earthquake. *Journal of Geophysical Research: Solid Earth*, 121, 3978–3995. <https://doi.org/10.1002/2015JB012417>
- Ripperger, J., & Mai, P. (2004). Fast computation of static stress changes on 2D faults from final slip distributions. *Geophysical Research Letters*, 31, L18610. <https://doi.org/10.1029/2004gl020594>
- Roesner, A., Ikari, M. J., Saffer, D. M., Stanislawski, K., Eijssink, A. M., & Kopf, A. J. (2020). Friction experiments under in-situ stress reveal unexpected velocity-weakening in Nankai accretionary prism samples. *Earth and Planetary Science Letters*, 538, 116180. <https://doi.org/10.1016/j.epsl.2020.116180>
- Sathiakumar, S., Barbot, S., & Hubbard, J. (2020). Earthquake cycles in fault-bend folds. *Journal of Geophysical Research: Solid Earth*, 125, e2019JB018557. <https://doi.org/10.1029/2019JB018557>
- Scholz, C. H. (2019). *The mechanics of earthquakes and faulting*. Cambridge University Press.
- Seeber, L., & Pêcher, A. (1998). Strain partitioning along the Himalayan arc and the Nanga Parbat antiform. *Geology*, 26, 791–794. [https://doi.org/10.1130/0091-7613\(1998\)026<0791:spatha>2.3.co;2](https://doi.org/10.1130/0091-7613(1998)026<0791:spatha>2.3.co;2)
- Smith, R. (1990). Tertiary plate tectonic setting and evolution of Papua New Guinea. Papua New Guinea (PNG) Petroleum Convention Proceedings.
- Stein, R. S., & King, G. C. (1984). Seismic potential revealed by surface folding: 1983 Coalinga, California, earthquake. *Science*, 224, 869–872. <https://doi.org/10.1126/science.224.4651.869>
- Tizzani, P., Castaldo, R., Solaro, G., Pepe, S., Bonano, M., Casu, F., et al. (2013). New insights into the 2012 Emilia (Italy) seismic sequence through advanced numerical modeling of ground deformation InSAR measurements. *Geophysical Research Letters*, 40, 1971–1977. <https://doi.org/10.1002/grl.50290>
- Tregoning, P., Lambeck, K., Stoltz, A., Morgan, P., McClusky, S. C., van der Beek, P., et al. (1998). Estimation of current plate motions in Papua New Guinea from Global Positioning System observations. *Journal of Geophysical Research*, 103, 12181–12203. <https://doi.org/10.1029/97JB03676>
- Valenti, G. (1993). P'nyang field: Discovery and geology of a gas giant in the western Papuan Fold Belt, Western Province, Papua New Guinea. Papua New Guinea (PNG) Petroleum Convention Proceedings.
- Wallace, L. M., Kaneko, Y., Hreinsdóttir, S., Hamling, I., Peng, Z., Bartlow, N., et al. (2017). Large-scale dynamic triggering of shallow slow slip enhanced by overlying sedimentary wedge. *Nature Geoscience*, 10, 765–770. <https://doi.org/10.1038/ngeo3021>
- Wallace, L. M., Stevens, C., Silver, E., McCaffrey, R., Loratung, W., Hasiata, S., et al. (2004). GPS and seismological constraints on active tectonics and arc-continent collision in Papua New Guinea: Implications for mechanics of microplate rotations in a plate boundary zone. *Journal of Geophysical Research*, 109, B05404. <https://doi.org/10.1029/2003JB002481>
- Wang, K., & Bürgmann, R. (2020). Probing fault frictional properties during afterslip up-dip and down-dip of the 2017 Mw 7.3 Sarpol-e Zahab earthquake with space geodesy. *Journal of Geophysical Research: Solid Earth*, 125, e2020JB020319. <https://doi.org/10.1029/2020JB020319>
- Wang, K., & Fialko, Y. (2015). Slip model of the 2015 M-w 7.8 Gorkha (Nepal) earthquake from inversions of ALOS-2 and GPS data. *Geophysical Research Letters*, 42, 7452–7458. <https://doi.org/10.1002/2015GL065201>
- Wang, S., Xu, C., Li, Z., Wen, Y., & Song, C. (2020). The 2018 Mw 7.5 Papua New Guinea earthquake: A possible complex multiple faults failure event with deep-seated reverse faulting. *Earth and Space Science*, 7, e2019EA000966. <https://doi.org/10.1029/2019ea000966>
- Wegmüller, U., Werner, C., Strozzi, T., Wiesmann, A., Frey, O., & Santoro, M. (2016). Sentinel-1 support in the GAMMA software. *Procedia Computer Science*, 100, 1305–1312.
- Wessel, P., Luis, J. F., Uieda, L., Scharroo, R., Wobbe, F., Smith, W. H., & Tian, D. (2019). The generic mapping tools version 6. *Geochemistry, Geophysics, Geosystems*, 20(11), 5556–5564.
- Xu, G., Xu, C., Wen, Y., & Yin, Z. (2019). Coseismic and postseismic deformation of the 2016 Mw 6.2 Lampa earthquake, Southern Peru, constrained by Interferometric Synthetic Aperture Radar. *Journal of Geophysical Research: Solid Earth*, 124, 4250–4272. <https://doi.org/10.1029/2018JB016572>
- Xu, W. (2017). Finite-fault slip model of the 2016 Mw 7.5 Chiloé earthquake, southern Chile, estimated from Sentinel-1 data. *Geophysical Research Letters*, 44, 4774–4780. <https://doi.org/10.1002/2017GL073560>
- Xu, X., Tong, X., Sandwell, D. T., Milliner, C. W. D., Dolan, J. F., Hollingsworth, J., et al. (2016). Refining the shallow slip deficit. *Geophysical Journal International*, 204, 1843–1862. <https://doi.org/10.1093/gji/ggv563>
- Yu, C., Li, Z., & Penna, N. T. (2018). Interferometric Synthetic Aperture Radar atmospheric correction using a GPS-based iterative tropospheric decomposition model. *Remote Sensing of Environment*, 204, 109–121. <https://doi.org/10.1016/j.rse.2017.10.038>
- Zhang, X., Feng, W., Du, H., Li, L., Wang, S., Yi, L., & Wang, Y. (2020). The 2018 MW 7.5 Papua New Guinea earthquake: A dissipative and cascading rupture process. *Geophysical Research Letters*, 47, e2020GL089271. <https://doi.org/10.1029/2020GL089271>